JACS
JOURNAL OF THE AMERICAN CHEMICAL SOCIETY

ARTICLE

pubs.acs.org/JACS

Controlling Nanocrystal Superlattice Symmetry and Shape-Anisotropic Interactions through Variable Ligand Surface Coverage

Joshua J. Choi,[†] Clive R. Bealing,[‡] Kaifu Bian,[§] Kevin J. Hughes,[§] Wenyu Zhang,[§] Detlef-M. Smilgies,[∥] Richard G. Hennig,[‡] James R. Engstrom,[§] and Tobias Hanrath*[,§]

[†]School of Applied and Engineering Physics;[‡]Department of Materials Science and Engineering; [§]School of Chemical and Biomolecular Engineering; [∥]Cornell High Energy Synchrotron Source. Cornell University, Ithaca, New York 14853, United States

Supporting Information

ABSTRACT: The assembly of colloidal nanocrystals (NCs) into superstructures with long-range translational and orientational order is sensitive to the molecular interactions between ligands bound to the NC surface. We illustrate how ligand coverage on colloidal PbS NCs can be exploited as a tunable parameter to direct the self-assembly of superlattices with predefined symmetry. We show that PbS NCs with dense ligand coverage assemble into face-centered cubic (fcc) superlattices whereas NCs with sparse ligand coverage assemble into body-centered cubic (bcc) superlattices which also exhibit orientational ordering of NCs in their lattice sites. Surface chemistry characterization combined with density functional theory calculations suggest that the loss of ligands occurs preferentially on {100} than on reconstructed {111} NC facets. The resulting anisotropic ligand distribution amplifies the role of NC shape in the assembly and leads to the formation of superlattices with translational and orientational order.

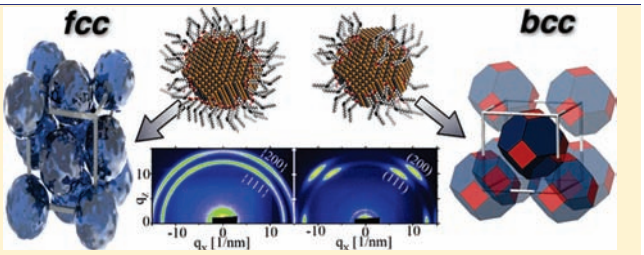

INTRODUCTION

The assembly of nanocrystals (NCs) into ordered superstructures is forecast to yield a new class of materials, also referred to as *artificial* solids, with tunable optical, electrical, and magnetic properties.[1,2] Most proposed NC-based technologies depend on functional assemblies in which the constituent NCs interact with each other and macroscopic external contacts. Therefore, controlling the structure of the NC assembly is both a valuable degree of freedom to gain fundamental insights into tunable collective properties of the NC ensemble and a critical requirement for the development of NC based technologies.[1,3,4] Compared to the growing body of knowledge on properties of individual NCs, progress in understanding the mechanisms underlying the formation of various NC assemblies and the relationship between superlattice structure and its collective properties has lagged behind.

Challenges to building the foundational understanding of mechanisms governing NC assembly formation arise primarily from the inherent complexity of the self-assembly process. NC superlattice self-assembly resides naturally at the intersection of molecular crystal growth and the assembly of micrometer-sized colloids. A number of interactions between the NCs, the surface-bound ligands and the surrounding solvent need to be considered.[5−8] To a first approximation, the interaction between colloidal NCs can be described by a soft sphere model which assumes isotropic NC interaction potentials and thus predicts the formation of close-packed (i.e., face-centered cubic, fcc or hexagonal close-packed, *hcp*) assemblies. The effective "softness" of the NC/ligand complex and the shape of the NC core introduce important perturbations that can lead to the formation of superlattices with non-close-packed (e.g., body-centered cubic, bcc) symmetry.[9−12] Electrostatic interactions must also be considered; for example, Talapin et al.[13] recently attributed the formation of NC assemblies with non-close-packed simple hexagonal (*sh*) symmetry to perturbations introduced by the electrostatic interactions between permanent NC dipoles. In a separate report, we show that NCs with identical core and ligand can be assembled into predefined superlattices with either *fcc,* body centered-tetragonal (bct), or bcc symmetry with orientational order of NCs in their lattice site.[14] This work underscored the significance of the molecular-level understanding of the role of ligand−ligand and ligand−solvent interactions in the self-assembly process.

Here, we show that the ligand coverage on the NC surface presents another important parameter in understanding and directing NC superlattice assembly. We discovered a relationship between ligand coverage density and superlattice symmetry and interpret the trend in context of anisotropic changes in the ligand coverage on specific NC facets. In this model, changes in surface chemistry amplify the effect of aspherical shape of NC on the interaction potential and lead to superlattices with long-range translational *and* orientational order. The interpretation of our experimental observations is corroborated by density functional theory (DFT) calculations of the ligand binding strength on

Received: November 20, 2010
Published: February 09, 2011

dx.doi.org/10.1021/ja110454b | *J. Am. Chem. Soc.* 2011, 133, 3131–3138

specific NC facets. Taken together, our experimental and computational results illustrate that facet-specific ligand surface coverage can change the asphericity of the NC-ligand complex and thereby control the symmetry of the resulting NC superlattice.

EXPERIMENTAL SECTION

NC Synthesis. The PbS synthesis was adopted from the work by Hines and Scholes.[15] PbO (1 mmol) and oleic acid (25 mmol) were dissolved in approximately 2 mL of Octadecene (ODE) to yield a solution with a total volume of 10 mL. The solution was then degassed by heating to 150 °C for 1 h under flowing nitrogen. In a glovebox, 0.6 mol of bis(trimethylsilyl)sulfide (TMS) was dissolved in 6 mL of ODE and stirred thoroughly. Five milliliters of the TMS solution was rapidly injected into the vigorously stirred, hot lead oleate solution. PbS NCs formed immediately after injection and, after 1 min of reaction at 150 °C, the reaction solution was cooled to room temperature and collected. Following the synthesis, the NCs were washed several times by sequential precipitation with ethanol and redispersion in anhydrous hexane.

NC Superlattice Formation. Silicon substrates were cleaned by sequential sonication in deionized water and acetone followed by ozone plasma treatment for 10 min. NC films were prepared by drop-casting 50 μL of 5 mg/mL NC suspension in hexane onto a cleaned 10 × 10 mm silicon substrate and drying the film in a controlled vapor environment. Details of the drop-casting deposition setup are given elsewhere.[16]

X-ray Scattering Characterization. Grazing incidence small-angle X-ray scattering (GISAXS) measurements were performed on beamline D1 of the Cornell High Energy Synchrotron Source (CHESS) using monochromatic radiation of wavelength $\lambda = 1.211$ Å with a bandwidth $\Delta\lambda/\lambda$ of 1.5%. The X-ray beam was produced by a hardbent dipole magnet of the Cornell storage ring and monochromatized with Mo:B_4C synthetic multilayers with a period of 30 Å. The D1 area detector (MedOptics) is a fiber-coupled CCD camera with a pixel size of 46.9 μm by 46.9 μm and a total of 1024 × 1024 pixels with a 14-bit dynamical range per pixel. Typical read-out time per image was below 5 s. The images were dark current corrected, distortion-corrected, and flat-field corrected by the acquisition software. The sample to detector distance was 1015 mm, as determined using a silver behenate powder standard. The incident angle of the X-ray beam was 0.25° i.e., slightly above the silicon critical angle. Typical exposure times ranged from 0.1 to 1.0 s. Scattering images were calibrated and integrated using the Fit2D software. GISAXS diffraction peaks were indexed and fitted using in-house software.[17] Grazing-incidence wide-angle x-ray scattering (GIWAXS) images were taken using a GE FLA-7000 image plate system. The image plate was moved into the beam after the superlattice structure had been established with GISAXS.

TEM Characterization. TEM samples were prepared by drop casting diluted NC solutions onto carbon coated 300 mesh Cu TEM grids. TEM images were taken on either an FEI Tecnai 20 (type Sphera) operated with a 200 kV LaB_6 filament or an FEI Titan equipped with a 300 kV field emission gun.

Surface Chemistry Characterization. Fourier transform infrared (FTIR) spectra were measured to probe the density of organic ligand bound to the NC surface. NC dispersions in tetrachloroethylene were put in a 3 mm path length quartz cuvette, and FTIR spectra were taken with Bruker Optics Vertex80v in vacuum mode. X-ray photoelectron spectroscopy was applied to probe the nature of the inorganic NC surface. XPS data was collected using an Omicron Sphera U5 concentric hemispherical electron energy analyzer (Omicron Nanotechnology USA, Eden Prairie, MN), operated at a constant pass energy of 50 eV. Nonmonochromated Mg Kα X-rays (1253.6 eV excitation energy) were produced using an Omicron DAR 400 twin anode source operated at 300 W (15 kV anode potential × 20 mA emission current). Pb(4f) spectra were fit assuming a spin−orbit doublet separation of 4.9 eV[18−20] with a fixed ratio of 3:4 for the $4f_{5/2}$ to $4f_{7/2}$ peak area. The full-width at half-maximum (fwhm) of all peaks was set to 1.58 eV, based on earlier measurements of a pure PbSe substrate (unpublished result). Error values given in the text refer to error originating from the fitting of XPS data only. Additional sources of error include uncertainty in the atomic sensitivity as well as photoelectron attenuation effects, which are complicated in the case of a highly 3-D film structure. These effects are expected to be similar for both films, so although the absolute uncertainty of the atomic ratios may be high, the relative uncertainty is low, and is reflected in the error values given in the text. Atomic ratios were calculated using atomic sensitivity values published previously.[21]

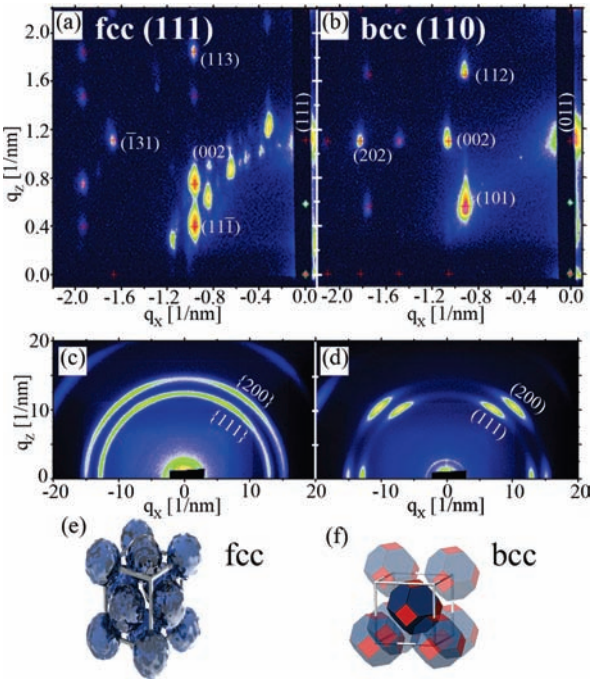

Figure 1. (a) N_2-aged PbS NCs formed an fcc superlattice with $(111)_{SL}$ planes parallel to the substrate, as shown by GISAXS. The associated GIWAXS pattern (c) shows at best weak orientational ordering of individual NCs. (b) Air-aged PbS NCs form bcc superlattice with $(110)_{SL}$ planes parallel to the substrate and with strong alignment of individual NCs (d). Schematic model of (e) fcc and (f) bcc superlattice with orientational coherence of individual NCs. The red shaded $\{100\}_{NC}$ are characterized by reduced ligand coverage as discussed in the text.

Computational Model of Ligand Bound to NC Surface. Density functional theory (DFT) was applied to calculate the binding strength of lead acetate to specific $\{100\}_{NC}$ and reconstructed $\{111\}_{NC}$ facets of the NC. Details on the DFT method are provided in the Supporting Information.

RESULTS AND DISCUSSION

The X-ray scattering results summarized in Figure 1 show that colloidal NC suspensions from the same synthesis batch can self-assemble to form superlattices with either fcc or bcc symmetry depending on the extent of air exposure of the colloidal suspension. We aged a 5 mg/mL hexane suspension of oleic acid (OA) passivated PbS NC inside a capped glass vial under ambient air and ambient light. The suspension was returned to the glovebox, and NCs were precipitated with ethanol, centrifuged to remove unbound ligand and finally redispersed in hexane. A control sample suspension from the same synthesis batch was aged inside a nitrogen glovebox (oxygen concentration <1 ppm) for the same period (four months) and washed with the same protocol. Using a previously reported method,[16] NC assemblies were

dx.doi.org/10.1021/ja110454b |J. Am. Chem. Soc. 2011, 133, 3131–3138

formed via drop-casting in a solvent saturated environment on top of cleaned silicon substrates (see Experimental Section for details). Similar experiments with shorter air exposure periods showed that suspensions exposed to air for only 2 days assembled into bct superlattice symmetry while bcc NC superlattice were formed from colloidal suspensions exposed to 6 days of ambient air (see Supporting Information). We note that the fcc−bct−bcc superlattice symmetry transformation is related through a Bain distortion as discussed in a separate report by our group.[14]

The grazing incidence small-angle X-ray scattering (GISAXS) pattern of the control PbS NC film (i.e., aged in nitrogen) shown in Figure 1a can be uniquely indexed to a highly ordered superlattice with fcc symmetry with $\{111\}_{SL}$ planes oriented parallel to the substrate. The subscripts "SL" and "NC" refer to the crystallographic planes and direction of the superlattice and individual nanocrystals respectively. The superlattice constant, a_{fcc}, of this assembly is measured to be 13.9 nm, and the lattice exhibits approximately 8% shrinkage in the vertical direction (normal to the substrate). Similar uniaxial lattice shrinkage has been observed in a number of different systems cast from solution, such as block copolymers,[22] nanocomposites,[23] and NC superlattices,[24−26] and seems to be a common feature of soft materials that are cast from solution.

Remarkably, air-aged NCs assembled to form a different superlattice symmetry than the fcc assembly observed in the nitrogen-aged control sample. The GISAXS pattern of NC assemblies formed from air-aged NCs reveals the scattering signature of crystal symmetry indexed to a bcc symmetry with $\{110\}_{SL}$ planes parallel to the substrate (Figure 1b). The bcc superlattice constant, a_{bcc}, is 11.0 nm, and the structure exhibits approximately 3% shrinkage in the vertical direction. The typical grain size of the fcc and bcc NC superlattice is on the order of 100−130 nm based on Scherrer equation analysis of the scattering peak width.[14,16]

To compare the different superlattice symmetries revealed by the GISAXS patterns, we analyzed the nearest-neighbor separation and the packing density (NC per unit volume). We determined the nearest neighbor separation by analyzing the spacing between NC surfaces, δ_{hkl}, along the $[hkl]$ close-packed direction of the superlattice. In fcc crystals the close-packed directions are the face diagonals $\langle 110\rangle$, hence the shortest separation between the surfaces of neighboring NCs is given by $\delta_{110} = ((2)^{1/2}/2)a_{fcc} - d_{NC}$, where d_{NC} is the average NC diameter determined from statistical analysis of TEM images (*vide infra*). In the case of the fcc superlattice formed from N_2-aged NCs, this spacing is 3.5 ± 0.6 nm, which corresponds to approximately twice the length of OA molecules (∼1.8 nm). We find a similar nearest-neighbor separation in the bcc superlattice (3.4 ± 0.7 nm); in this case the close-packed directions are along the body diagonals $\langle 111\rangle$ and the corresponding inter-NC separation is given by $\delta_{111} = ((3)^{1/2}/2)a_{bcc} - d_{NC}$. Both fcc and bcc NC superlattices are characterized by a packing density of approximately ($\rho \sim 1.49(10^{18})$ NC cm^{-3}). From the perspective of the hard-sphere model, this result is surprising since the theoretical volume packing fraction of *hard* spheres in a fcc crystal (0.74) is significantly larger than for a bcc crystal (0.68). However, note that the observed fcc and bcc lattice constants differ significantly, with the effect that NC density and thickness of the ligand sphere come out very similar. This implies that the observed structural differences must be due to differences in the ligand-mediated short-range repulsive interaction between adjacent particles.

To better understand how superlattice symmetry is related to the shape and orientation of individual NC within the lattice, we simultaneously measured grazing-incidence wide-angle X-ray scattering (GIWAXS). The GIWAXS pattern of the fcc superlattice formed from N_2-aged NCs shows ringlike scattering patterns, which indicates that individual NCs are randomly oriented within their superlattice sites (Figure 1c). In contrast, bcc superlattices formed from air-aged NCs showed $(111)_{NC}$ and $(200)_{NC}$ reflections with narrow azimuthal widths in the GIWAXS pattern. This scattering indicates orientational ordering of individual NCs in their lattice sites (Figure 1d). Specifically, we find that the $[110]_{NC}$ axis of PbS NCs within the superlattice is oriented coaxially with the $[110]_{SL}$ direction of the bcc superlattice. Figures 1e and 1f schematically illustrate the translational and orientational order in the NC fcc and bcc superlattices.

Taken together, the small-angle and wide-angle X-ray scattering data provide important insights on the effective shape of the interaction volume of the NC core/surface ligand complex. The combination of long-range translational and orientational ordering in the bcc superlattices cannot be explained with the NCs modeled as soft spheres. Instead, orientational coherence of NCs within the superlattice indicates an aspherical interaction potential. More precisely, the NCs in the air-aged suspension interact as truncated octahedrons. Note that the special case of a truncated octahedron is the Wigner−Seitz cell of the bcc superlattice which can be packed with 100% space filling density in a bcc crystal. NCs in the N_2-aged suspensions on the other hand assemble into an fcc superlattice without orientational coherence; in this case quasi-spherical NC approximation adequately describes the symmetry of the interaction potential.

The observation of different superlattice symmetries leads to the intriguing question: why do colloidal NCs aged under different conditions self-assemble into different superlattice symmetries? To answer this question we formulated the following three alternative hypotheses:

1. NC Size, Shape and Charged Facets. Figures 2a and 2b show transmission electron microscopy (TEM) images and statistical image analysis of NC monolayers prepared from the colloidal suspensions aged in nitrogen and air, respectively. Air-aged NCs exhibited a slightly smaller NC diameter (6.1 ± 0.7 nm) compared to the N_2-aged NCs (6.3 ± 0.6 nm). We note that the extent of reduction of the average PbS NC diameter is less pronounced than that of a recent report by Sykora et al.[27] in the case of PbSe NCs. Moreover, our PbS NC suspension remained stable for the four-month time frame considered in our aging experiments and excessive aggregation was not observed. Differences in the comparison of PbS and PbSe NCs likely arise from variations in NC surface chemistry, synthesis and cleaning protocols, NC concentration and light exposure.[28] The TEM analysis summarized in Figure 2 allows us to eliminate changes in the NC core size and shape as the driving force behind the superlattice symmetries.

2. NC Dipoles and Electrostatic Charging Due to Ligand Loss. As an alternative hypothesis, we also considered the possibility of an aspherical interaction potential arising from NC dipoles or more generally Coulombic interactions of charged NCs. We tested the electrophoretic mobility of NCs with different ligand coverage and observed no significant correlation between the electrophoretic mobility and the NC ligand coverage (Supporting Information). This suggests that possible differences in the nature of charged surface states are either absent or below the measurement sensitivity.

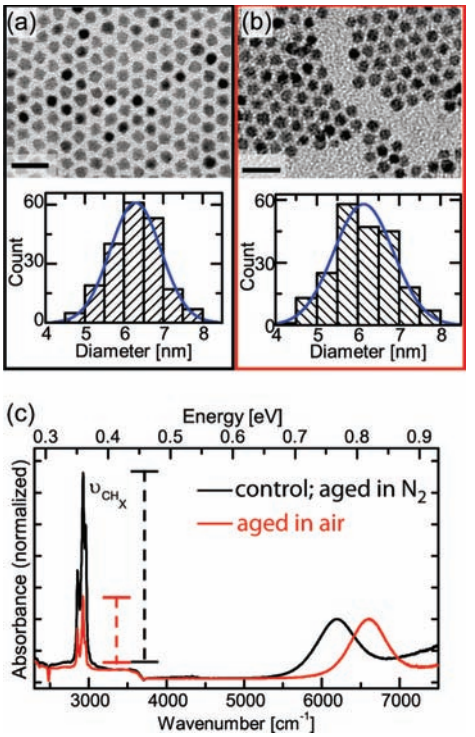

Figure 2. TEM images and histogram of NC size analysis of suspensions aged in nitrogen (a) and in air (b). The scale bars correspond to 10 nm. (c) FTIR spectrum of colloidal PbS NC suspensions. Suspensions aged in air show a decreased intensity of C−H vibrations due to reduced ligand coverage and a blue shift in the exciton peak of the NC core.

3. NC Surface Chemistry and Molecular Interactions of Surface Bound Ligands. NC surface ligand coverage can be determined using infrared spectroscopy. Fourier transform infrared (FTIR) spectra of colloidal PbS NCs dispersed in tetrachloroethylene show two distinct features: (i) the C−H vibrational signatures (υ_{CH}; near 2900 cm^{-1}) of the OA ligand and (ii) the exciton peak (E_G; ~6000−7000 cm^{-1}) of the quantum confined NC core (Figure 2c). Consistent with other reports,[27−29] we observe a blue-shift of the NC exciton peak in response to air exposure, which suggests that air-aged NCs are characterized by stronger quantum confinement, i.e. a decrease in the volume of the PbS NC to which the wave functions are confined.[30] Based on the well-established relationship between NC size and energy gap (E_G),[31−33] we can correlate the 0.05 eV blue shift of the exciton peak with reduction in NC core size by approximately 0.4 nm, which is in good agreement with the TEM analysis.

We can use the relative intensity of the ligand stretching (υ_{CH}) and NC core excitation (E_G) spectral signatures to directly assess the ratio (ϕ) of OA ligands per NC. We calibrated peak height of υ_{CH} from the NC suspension relative to standardized solutions with known OA concentration and determined the NC concentration from size-dependent extinction coefficient of PbS NCs[34] (detailed calculations are provided in the Supporting Information). Using this approach we found that the N_2-aged NCs had a ligand coverage of approximately 4.5 ± 0.7 nm^{-2} whereas the air-aged NCs had a 60% lower coverage (~1.8 ± 0.3 nm^{-2}). We emphasize that the calculated ligand density should be taken as an upper bound estimate since the actual surface area of the NC depends on the specific shape and surface faceting. Similar calculations for truncated octahedron shaped NCs result in approximately 10% lower coverage density due to larger overall surface compared to spheres of equal volume (see Supporting Information). Our calculated ligand coverage agrees well with a previous report by Moreels et al.[29] in which they presented extensive studies on surface chemistry of PbSe NCs and observed a similar surface ligand density of 4.2 nm^{-2} and 40% ligand loss due to 2 months of air exposure.

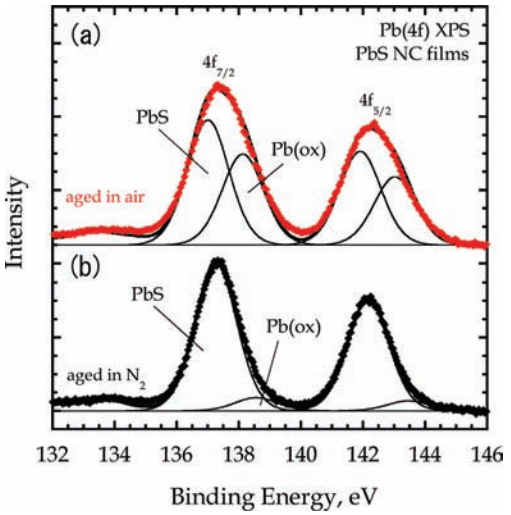

Figure 3. X-ray photoelectron spectra of films of air-aged (a) and N_2-aged (b) PbS NCs. Spectra were fit assuming contributions from two chemical binding environments, one corresponding to PbS, the other to a more highly oxidized form of Pb. In the air-aged case, the more highly oxidized form accounts for 42% of the total area of the feature, while for the N_2 aged case the more highly oxidized form accounts for 8% of the total. The spectrum for air-aged NCs has been shifted higher on the ordinate to facilitate presentation.

We conjectured that the reduced surface coverage in air-aged NC suspensions results from changes in the composition of the NC surface (e.g., partial oxidation) that may reduce the affinity of the ligand to the oxidized NC surface. The oxidized species formed on different NC facets are likely to be dissimilar vis-à-vis the differences in surface termination and reconstruction: the precise reconstruction and faceting is not yet fully understood and remains a subject of intensive investigation.[35,36] We turned to X-ray photoelectron spectroscopy (XPS) to investigate changes in the chemical composition of the PbS NCs. XP spectra were collected from thin films of NCs drop-cast onto cleaned silicon substrates (exposure to ambient air was limited to less than 5 min during loading into the XPS chamber). We note that, considering the inelastic mean free path of the O(1s), Pb(4f), and S(2s) photoelectrons in PbS (1.8−2.6 nm),[37] XPS analysis gives disproportionate weight to the atoms on the outer surface of the particles, and that the majority of signal will be from the top few NC layers.

XP spectra from the Pb(4f) region for the air-aged and N_2-aged PbS NC films are displayed in Figure 3. Here the data is fit to two peak doublets: one attributed to Pb atoms in a sulfide binding environment (PbS), the other to Pb in a more highly oxidized state [Pb(ox)]. The difference in binding energies of the PbS and Pb(ox) peaks was 1.1 and 1.3 eV for the air-aged and N_2-aged samples, respectively. A number of oxidation products resulting in shifts in the Pb(4f) binding energy in the range of +0.9 to +1.5 eV are possible, depending on the conditions and the extent of surface exposure to the oxidizing agents.[38−40] Therefore, we will not assign a specific chemical structure to

dx.doi.org/10.1021/ja110454b | J. Am. Chem. Soc. 2011, 133, 3131–3138

the high binding energy peak, though the most likely components are PbO, $Pb(OH)_2$, and $PbCO_3$.[38−40] In the air-aged NCs, the oxidized species accounts for 42% of the total area of the Pb(4f) feature, whereas for the N_2-aged film the oxidized species account for only 8%. In addition, the O/Pb atomic ratio was calculated to be 1.27 for the air-aged particles, and 0.91 for the N_2-aged particles (see Supporting Information for details of XPS peak fitting and atomic ratio calculation). Taken together, the Pb(4f) peak fitting and the O/Pb ratio indicate that a higher proportion of lead atoms are oxidized in the air-aged NC film.

Inspection of the S(2s) feature for the air-aged particles indicates that no significant S-containing oxidation products are present (Supporting Information). For extensive air exposures, planar PbS is known to form sulfate species, which would be observed at ~7 eV above the sulfide component.[41] However, this was not observed in our NC films. Notably, the S/Pb ratio was found to be 0.35 for the air-aged and 0.52 for the N_2-aged NCs. Simultaneous increase in the oxygen content, the appearance of a high-binding energy component in the Pb(4f) feature, and a decrease in the S/Pb atomic ratio have been observed previously during the early stages of planar PbS oxidation.[38] The decrease in the S/Pb ratio upon oxidation likely indicates that the sulfur-containing oxidation products of PbS have sufficiently high vapor pressure to leave the surface under ultrahigh vacuum, or react with air prior to introduction into the vacuum chamber. Previous XPS studies have shown that elemental sulfur, for example, is only detected on the oxidized PbS surface if the sample is cooled to <150 K while under vacuum.[38] The ~33% decrease in relative S concentration, along with the increase of ~34% in the relative contribution of Pb(ox) to the Pb(4f) feature suggests that the near-surface sulfur atoms are being replaced by atmospheric O from O_2, H_2O, or CO_2.

The partial oxidation of PbS NC surfaces indicated by the XPS study is qualitatively consistent with the reduced OA ligand coverage evidenced by the FTIR spectra. The oxidation of surface lead atoms would be accompanied by loss of oleate ligands based on a previous XPS analysis of PbS NC by Weller and co-workers that showed oleate binding to surface lead atoms.[42] Since the species and extent of oxidation across different NC facets may be different, it is likely that the detachment of ligand may also be more pronounced on specific NC facets. At present, the precise determination of ligand coverage on specific NC facets is beyond the capabilities of state-of-the-art characterization tools.

To get a better understanding of the physical and chemical nature of the NC surface at atomic length scales, we turned to computational model and DFT analysis of ligand binding energies on different facets (Figure 4). We modeled $\{100\}_{NC}$ and $\{111\}_{NC}$ surfaces with atomic details and calculated binding energies of Pb acetate ($Pb(CH_3COO)_2$) on each facet (see Experimental section and Supporting Information for detailed DFT methods). $Pb(CH_3COO)_2$ was chosen instead of Pb oleate[29,42] for increased computational efficiency. The functional group, rather than the carbon chain length, is expected to dominate the binding.

PbS NC surfaces were modeled with slabs consisting of four layers; only the atoms in the top layer were allowed to move during relaxation. For the $\{001\}_{NC}$ surface, the cations and anions in the surface layer relaxed slightly inward, reducing the layer spacing from the bulk value of 3.00 Å to about 2.82 Å. For the $\{111\}_{NC}$ surface, the occurrence of a surface reconstruction was taken into account. Unreconstructed $\{111\}_{NC}$ surfaces exhibit a very high surface energy.[35] The $\{111\}_{NC}$ layers are composed of oppositely charged layers of cations and anions resulting in a dipole moment perpendicular to the plane. Recently, Fang et al.[35] showed that the surface energy of $\{111\}_{NC}$-terminated PbSe surfaces is reduced by more than an order of magnitude if alternating rows of cations in the topmost layer are removed. As such, each surface terminates in half a monolayer of cations above a full layer of anions; this approach to the reconstruction (referred from here on as the $\{111\}_{NC}$-1/2-Pb reconstruction) has long been known to drastically reduce the surface energy of other polar ionic crystal surfaces.[43] Rutherford backscattering experiments suggest that real PbSe $\{111\}_{NC}$ surfaces may be reconstructed along these lines; epitaxially grown PbSe was seen to terminate in a Pb layer which had an atomic density of about 40%.[44] After relaxation of the $\{111\}_{NC}$-1/2-Pb reconstructed surface, the Pb atoms in the terminating layer shift slightly closer to the remainder of the slab, such that the separation between the surface Pb atoms and the neighboring S atoms is 2.6−2.8 Å.

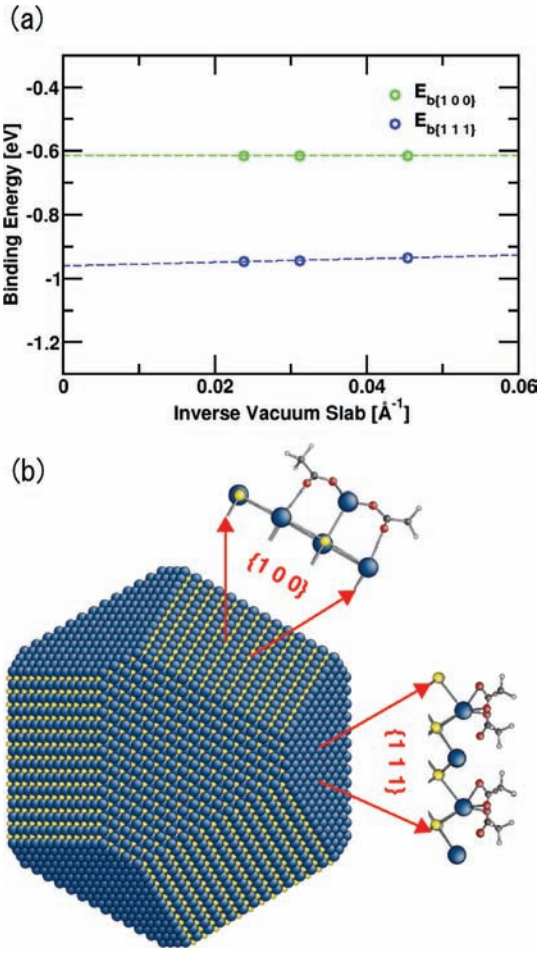

Figure 4. Density functional theory calculations of Pb-acetate molecule binding energies to the PbS {111} (blue), and {100} (green) surfaces. {111} surfaces were modeled to account for surface reconstruction (see the main text for details). This result indicates that the Pb-oleate ligands bind stronger to $\{111\}_{NC}$ facets than $\{100\}_{NC}$ facets and provide important insights on facet specific ligand adsorption/detachment equilibrium.

The binding energy of $Pb(CH_3COO)_2$ on the reconstructed $\{111\}_{NC}$ surface is calculated by placing the Pb atom of $Pb(CH_3COO)_2$ inside the "trench" resulting from the surface

dx.doi.org/10.1021/ja110454b | J. Am. Chem. Soc. 2011, 133, 3131–3138

reconstruction, while for the $\{001\}_{NC}$ slab, the Pb atom was placed above a surface S atom. In both cases a number of initial geometries for the acetate molecules were attempted, in order to find the geometry with the strongest binding energy in each case. The modeled $Pb(CH_3COO)_2$ molecules absorbed on $\{001\}_{NC}$ and $\{111\}_{NC}$ surfaces, after the system has been relaxed using DFT, are shown in the Supporting Information. The binding energies for $Pb(CH_3COO)_2$ on the $\{001\}_{NC}$ and the reconstructed $\{111\}_{NC}$ surfaces were calculated to be 0.616 ± 0.017 eV and 0.962 ± 0.012 eV, respectively.

Importantly, our DFT results indicate that the Pb-oleate ligands bind stronger to the $\{111\}_{NC}$ facets than to the $\{100\}_{NC}$ facets and provide important insights on facet specific ligand adsorption/detachment equilibrium. We emphasize here that organic ligands bound to the surface of an inorganic NC core constitute a dynamic system. These dynamics are a well-established concept underlying the controlled nucleation and growth processes during NC synthesis. Aside from stabilizing the growing NC, the ligand attachment to specific NC facets can be tailored to modify the relative growth rate of those facets and thereby enable the growth of nanostructures with complex 3-dimensional shapes.[45] At room temperature, the ligand dynamics in colloidal NC suspensions are slowed down considerably, but the dynamics between bound and unbound ligands still play an important role.[46] Indeed, Moreels et al. have observed this dynamic between bound and unbound lead oleate ligands on PbSe NCs.[29] Our DFT results therefore provide insights on facet specific ligand loss equilibrium dynamics and indicate anisotropic ligand loss across different NC facets: $\{100\}_{NC}$ facets will end up with reduced ligand coverage compared to the $\{111\}_{NC}$ facets.

In conjunction with the XPS data, the DFT results suggest another possible mechanism of facet specific ligand loss − anisotropic ligand loss due to facet specific oxidation. Lead salt NCs have been found to have a significant amount ($\sim$ 40%) of excess lead atoms.[47] Comparing calculated energies required to put excess lead atoms on $\{111\}_{NC}$ and $\{100\}_{NC}$ facets, we reason that the excess lead atoms are more likely to be distributed on $\{111\}_{NC}$ facets rather than $\{100\}_{NC}$ facets. The dense distribution of excess Pb atoms on $\{111\}_{NC}$ facets would bury the S atom layers underneath and thus block them from oxidation. This reasoning, along with our XPS data that show replacement of surface S atoms with O atoms, suggests that it is $\{100\}_{NC}$ facets that are more readily being oxidized and thus losing ligands.

Given the experimental and computational results discussed so far, we now discuss how the detailed spatial arrangement of OA ligands on specific NC facets influences interactions between NCs during self-assembly of the superlattice. If we consider a fully passivated NC with high ligand coverage, the dense ligand shell effectively masks the faceted shape of the NC core and neighboring NCs interact as soft spheres. On the other hand, lower surface coverage, especially due to anisotropic ligand loss across different facets, will enhance the NC shape effect and the anisotropy of the NC interaction volume. Variations in ligand coverage density resulting in "patchy" particles have previously been recognized as an important parameter in the directed self-assembly of colloids,[8] e.g. Janus particles,[48] or isolated DNA-functionalized metal nanoparticle homodimers.[49,50] Here, we illustrate that the anisotropic ligand coverage can also be exploited to control the translational and orientational order of NC superlattices.

The 8-fold coordination of NCs in the bcc superlattice and the 8-fold degeneracy of $\{111\}_{NC}$ facets of individual PbS NCs provides an important clue for understanding the relationship between facet specific ligand coverage and the assembly of the non-close-packed bcc structure. The relationship between NC faceting and orientational alignment is consistent with a recent molecular dynamics simulation by Fichthorn and Qin which illustrated that oscillatory solvation forces induce neighboring particles to rotate to approach each other via paths of minimum free energy.[51] Moreover, we note that the preferred interaction between $\{100\}_{NC}$ facets of neighboring PbS NCs is consistent with the oriented attachment of lead chalcogenide NCs into nanowires or nanorods.[52−55]

Considering the detailed molecular interactions between surface bound ligands, another possible mechanism is that ligands on $\{111\}_{NC}$ facets of neighboring NCs will, through van der Waals interaction, be interdigitated or aligned with each other to form "artificial bonds" to connect NCs along specific crystallographic directions. In case of the truncated octahedral NCs studied in this work, such "bonds" between ligands bound to $\{111\}_{NC}$ facets strengthen interactions along the 8-fold $\langle 111\rangle_{SL}$ directions. We note that this interpretation is similar to earlier molecular dynamics simulations by Landman and Luedtke who predicted that ligands bound to the surface of Au NCs arrange to form bundles.[56] The proposed formation of "ligand-bridges" connecting neighboring NCs, as previously reported by Wang for metal NC assemblies, is consistent with this picture.[57] Whether oleic acid ligands bound to the surface of PbS NCs form bundles is a subject of ongoing experimental and theoretical investigation in our laboratory.[14]

■ CONCLUSIONS

In summary, we show how variations in ligand coverage on specific NC facets may influence the interactions between NCs during assembly into ordered superstructures. PbS NCs with dense ligand coverage assemble into fcc superlattices. Reduced ligand coverage on aged and partially oxidized NCs assemble into bcc superlattices with orientational order. Our experimental and computational results indicate that the assembly of the aged NCs is influenced by anisotropic ligand coverage on $\{111\}_{NC}$ and $\{100\}_{NC}$ facets of truncated octahedral NCs. The anisotropic ligand coverage amplifies the significance of the NC core shape during assembly. Beyond the implications on NC superlattice with controlled symmetries illustrated in this paper, improved understanding of ligand coverage and surface chemistry on specific NC facets also provides important insights into the interactions responsible for the fusion of lead chalcogenide NCs into 1D wires,[52,53] rods,[54] or 2D sheets.[58]

■ ASSOCIATED CONTENT

Supporting Information. Superlattice structures formed from colloidal NC suspensions with short-term air exposure; assessment of ligand coverage density via FTIR spectroscopy; calibration of ligand concentration and calculation of surface coverage on spherical and faceted NCs; electrophoretic mobility measurements of colloidal NC suspensions, details of XPS analysis; details of DFT calculations; adjustment to NC ligand coverage via filtering and antisolvent treatment; and scanning and transmission electron micrographs of the NC films. This material is available free of charge via the Internet at http://pubs.acs.org.

■ AUTHOR INFORMATION

Corresponding Author
th358@cornell.edu

■ ACKNOWLEDGMENT

This work was supported in part by Award No. KUS-C1-018-02, made by King Abdullah University of Science and Technology (KAUST) and by the National Science Foundation, Award NSF-CBET 0828703. J.J.C. was supported by the NSF IGERT Fellowship Program on "Nanoscale Control of Surfaces and Interfaces," administered by Cornell's MRSEC. K.B. was supported by NSF-CBET 0828703. GISAXS measurements were conducted at the Cornell High Energy Synchrotron Source (CHESS), which is supported by the National Science Foundation and the National Institutes of Health/National Institute of General Medical Sciences under NSF Award DMR-0936384. This research used computational resources of the Computation Center for Nanotechnology Innovation at Rensselaer Polytechnic Institute and was supported in part by the National Science Foundation through TeraGrid computational resources provided by the National Center for Supercomputing Applications, the Texas Advanced Computing Center and under the Louisiana Optical Network Initiative under Grant No. DMR050036

■ REFERENCES

(1) Markovich, G.; Collier, C. P.; Henrichs, S. E.; Remacle, F.; Levine, R. D.; Heath, J. R. *Acc. Chem. Res.* **1999**, *32*, 415–423.
(2) Talapin, D. V.; Lee, J.-S.; Kovalenko, M. V.; Shevchenko, E. V. *Chem. Rev.* **2010**, *110*, 389–458.
(3) Remacle, F.; Levine, R. *ChemPhysChem* **2001**, *2*, 20–36.
(4) Pileni, M. P. *J. Phys. Chem. B* **2001**, *105*, 3358–3371.
(5) Bishop, K. J. M.; Wilmer, C. E.; Soh, S.; Grzybowski, B. A. *Small* **2009**, *5*, 1600–1630.
(6) Min, Y.; Akbulut, M.; Kristiansen, K.; Golan, Y.; Israelachvili, J. *Nat. Mater.* **2008**, *7*, 527–538.
(7) Pileni, M. P. *Acc. Chem. Res.* **2008**, *41*, 1799–1809.
(8) Grzelczak, M.; Vermant, J.; Furst, E. M.; Liz-Marzan, L. M. *ACS Nano* **2010**, *4*, 3591–3605.
(9) Whetten, R. L.; Shafigullin, M. N.; Khoury, J. T.; Schaaff, T. G.; Vezmar, I.; Alvarez, M. M.; Wilkinson, A. *Acc. Chem. Res.* **1999**, *32*, 397–406.
(10) Korgel, B. A.; Fitzmaurice, D. *Phys. Rev. B* **1999**, *59*, 14191–14191.
(11) Lu, W.; Liu, Q.; Sun, Z.; He, J.; Ezeolu, C.; Fang, J. *J. Am. Chem. Soc.* **2008**, *130*, 6983–6991.
(12) Henry, A.-I.; Courty, A.; Pileni, M.-P.; Albouy, P.-A.; Israelachvili, J. *Nano Lett.* **2008**, *8*, 2000–2005.
(13) Talapin, D. V.; Shevchenko, E. V.; Murray, C. B.; Titov, A. V.; Král, P. *Nano Lett.* **2007**, *7*, 1213–1219.
(14) Bian, K.; Choi, J. J.; Prakash, A.; Clancy, P.; Smilgies, D. M.; Hanrath, T. *ACS Nano* **2011** (accepted).
(15) Hines, M. A.; Scholes, G. D. *Adv. Mater.* **2003**, *15*, 1844–1849.
(16) Hanrath, T.; Choi, J. J.; Smilgies, D.-M. *ACS Nano* **2009**, *3*, 2975–2988.
(17) Smilgies, D.-M.; Blasini, D. R. *J. Appl. Crystallogr.* **2007**, *40*, 716–718.
(18) McGilp, J. F.; et al. *J. Phys. C: Solid State Phys.* **1977**, *10*, 3445.
(19) Nyholm, R.; et al. *J. Phys. C: Solid State Phys.* **1980**, *13*, L1091.
(20) Shalvoy, R. B.; Fisher, G. B.; Stiles, P. J. *Phys. Rev. B* **1977**, *15*, 1680–1680.
(21) Wagner, C. D.; Davis, L. E.; Zeller, M. V.; Taylor, J. A.; Raymond, R. H.; Gale, L. H. *Surf. Interface Anal.* **1981**, *3*, 211–225.
(22) Bosworth, J. K.; Paik, M. Y.; Ruiz, R.; Schwartz, E. L.; Huang, J. Q.; Ko, A. W.; Smilgies, D. M.; Black, C. T.; Ober, C. K. *ACS Nano* **2008**, *2*, 1396–1402.
(23) Crossland, E. J. W.; Kamperman, M.; Nedelcu, M.; Ducati, C.; Wiesner, U.; Smilgies, D.-M.; Toombes, G. E. S.; Hillmyer, M. A.; Ludwigs, S.; Steiner, U.; Snaith, H. J. *Nano Lett.* 2009, *9* (8), 2807–2812.
(24) Dunphy, D.; Fan, H. Y.; Li, X. F.; Wang, J.; Brinker, C. J. *Langmuir* **2008**, *24*, 10575–10578.
(25) Smith, D.; Goodfellow, B.; Smilgies, D.; Korgel, B. *J. Am. Chem. Soc.* **2009**, *131*, 3281–3290.
(26) Friedrich, H.; Gommes, C. J.; Overgaag, K.; Meeldijk, J. D.; Evers, W. H.; de Nijs, B.; Boneschanscher, M. P.; de Jongh, P. E.; Verkleij, A. J.; de Jong, K. P.; van Blaaderen, A.; Vanmaekelbergh, D. *Nano Lett.* **2009**, *9*, 2719–2724.
(27) Sykora, M.; Koposov, A. Y.; McGuire, J. A.; Schulze, R. K.; Tretiak, O.; Pietryga, J. M.; Klimov, V. I. *ACS Nano* **2010**, *4*, 2021–2034.
(28) Dai, Q.; Wang, Y.; Zhang, Y.; Li, X.; Li, R.; Zou, B.; Seo, J.; Wang, Y.; Liu, M.; Yu, W. W. *Langmuir* **2009**, *25*, 12320–12324.
(29) Moreels, I.; Fritzinger, B.; Martins, J. C.; Hens, Z. *J. Am. Chem. Soc.* **2008**, *130*, 15081–15086.
(30) Stouwdam, J. W.; Shan, J.; van Veggel, F. C. J. M.; Pattantyus-Abraham, A. G.; Young, J. F.; Raudsepp, M. *J. Phys. Chem. C* **2007**, *111*, 1086–1092.
(31) Murray, C.; Sun, S.; Gaschler, W.; Doyle, H.; Betley, T.; Kagan, C. *IBM J. Res. Dev.* **2001**, *45*, 47–56.
(32) Evans, C. M.; Guo, L.; Peterson, J. J.; Maccagnano-Zacher, S.; Krauss, T. D. *Nano Lett.* **2008**, *8*, 2896–2899.
(33) Yu, W.; Falkner, J.; Shih, B.; Colvin, V. *Chem. Mater.* **2004**, *16*, 3318–3322.
(34) Moreels, I.; Lambert, K.; Smeets, D.; De Muynck, D.; Nollet, T.; Martins, J. C.; Vanhaecke, F.; Vantomme, A.; Delerue, C.; Allan, G.; Hens, Z. *ACS Nano* **2009**, *3*, 3023–3030.
(35) Fang, C.; van Huis, M. A.; Vanmaekelbergh, D. l.; Zandbergen, H. W. *ACS Nano* **2010**, *4*, 211–218.
(36) Petkov, V.; Moreels, I.; Hens, Z.; Ren, Y. *Phys. Rev. B* **2010**, *81*, 241304–241304.
(37) Tanuma, S.; Powell, C. J.; Penn, D. R. *Surf. Interface Anal.* **1991**, *17*, 927–939.
(38) Buckley, A. N.; Woods, R. *Appl. Surf. Sci.* **1984**, *17*, 401–414.
(39) Nowak, P.; Laajalehto, K. *Appl. Surf. Sci.* **2000**, *157*, 101–111.
(40) Zingg, D. S.; Hercules, D. M. *J. Phys. Chem.* **1978**, *82*, 1992–1995.
(41) Evans, S.; Raftery, E. *J. Chem. Soc., Faraday Trans. 1* **1982**, *78*, 3545–3545.
(42) Lobo, A.; Moller, T.; Nagel, M.; Borchert, H.; Hickey, S.; Weller, H. *J. Phys. Chem. B* **2005**, *109*, 17422–17428.
(43) Kummer, J. T.; Yao, Y.-F. Y. *Can. J. Chem.* **1967**, *45*, 421.
(44) Kimura, K.; Nakajima, K.; Fujii, Y.; Mannami, M.-h. *Surf. Sci.* **1994**, *318*, 363–367.
(45) Kanaras, A. G.; Sonnichsen, C.; Liu, H.; Alivisatos, A. P. *Nano Lett.* **2005**, *5*, 2164–2167.
(46) Kim, B.; Avila, L.; Brus, L.; Herman, I. *Appl. Phys. Lett.* **2000**, *76*, 3715–3717.
(47) Moreels, I.; Lambert, K.; De Muynck, D.; Vanhaecke, F.; Poelman, D.; Martins, J. C.; Allan, G.; Hens, Z. *Chem. Mater.* **2007**, *19*, 6101–6106.
(48) Jiang, S.; Chen, Q.; Tripathy, M.; Luijten, E.; Schweizer, K. S.; Granick, S. *Adv. Mater.* **2010**, *22*, 1060–1071.
(49) Xu, X.; Rosi, N. L.; Wang, Y.; Huo, F.; Mirkin, C. A. *J. Am. Chem. Soc.* **2006**, *128*, 9286–9287.
(50) Maye, M. M.; Nykypanchuk, D.; Cuisinier, M.; van der Lelie, D.; Gang, O. *Nat. Mater.* **2009**, *8*, 388–391.
(51) Fichthorn, K. A.; Qin, Y. *Ind. Eng. Chem. Res.* **2006**, *45*, 5477–5481.
(52) Cho, K.-S.; Talapin, D. V.; Gaschler, W.; Murray, C. B. *J. Am. Chem. Soc.* **2005**, *127*, 7140–7147.
(53) Schapotschnikow, P.; van Huis, M. A.; Zandbergen, H. W.; Vanmaekelbergh, D.; Vlugt, T. J. H. *Nano Lett.* **2010**, *10*, 3966–3971.
(54) Koh, W.-k.; Bartnik, A.; Wise, F.; Murray, C. *J. Am. Chem. Soc.* **2010**, *132*, 3909–3913.
(55) Justo, Y.; Moreels, I.; Lambert, K.; Hens, Z. *Nanotechnology* **2010**, *21*, 295606.

(56) Luedtke, W. D.; Landman, U. *J. Phys. Chem.* **1996**, *100*, 13323–13329.
(57) Wang, Z. L. *Adv. Mater.* **1998**, *10*, 13–30.
(58) Schliehe, C.; Juarez, B. H.; Pelletier, M.; Jander, S.; Greshnykh, D.; Nagel, M.; Meyer, A.; Foerster, S.; Kornowski, A.; Klinke, C.; Weller, H. *Science* **2010**, *329*, 550–553.